RESEARCH ARTICLE

Check for updates

Tunable SIM properties in a family of 3D anilato-based lanthanide-MOFs†‡

Noemi Monni,§[a,b] Sourav Dey,§[a] Víctor García-López, [ID] [a] Mariangela Oggianu,[b] José J. Baldoví, [ID] [a] Maria Laura Mercuri, [ID] *[b] Miguel Clemente-León [ID] *[a] and Eugenio Coronado [ID] [a]

By reacting a 3,6-ditriazolyl-2,5-dihydroxybenzoquinone (H_2trz_2An) anilato linker with Ln^{III} ions (Ln^{III} = Dy, Tb, Ho), two different series of polymorphs, formulated as $[Ln_2(trz_2An)_3(H_2O)_4]_n \cdot 10H_2O$ (Dy^{III}, **1a**; Tb^{III}, **2a**, Ho^{III}, **3a**) and $[Ln_2(trz_2An)_3(H_2O)_4]_n \cdot 7H_2O$ (Dy^{III}, **1b**, Tb^{III}, **2b**, Ho^{III}, **3b**) have been obtained. In these series the two Dy^{III}-coordination networks (**1a** and **1b**) and the Tb^{III}-coordination polymer (**2b**) show a Single Ion Magnet (SIM) behavior. **1–3a** MOFs show reversible structural flexibility upon removal of a coordinated water molecule from a distorted hexagonal 2D framework to a distorted 3,6-brickwall rectangular 3D structure in $[Ln_2(trz_2An)_3(H_2O)_2]_n \cdot 2H_2O$ (Dy^{III}, **1a_des**; Tb^{III}, **2a_des**, Ho^{III}, **3a_des**) involving shrinkage/expansion of the hexagonal–rectangular networks. Noteworthy, **2b** represents the first example of a Tb^{III}–anilate-based coordination polymer showing SIM behaviour to date and the best SIM properties within the polymorphs. Theoretical investigation *via ab initio* CASSCF calculations supports this behavior, since **2b** shows less mixing between the m_J states of the ground state among all the studied complexes.

Introduction

Metal–Organic Frameworks (hereafter MOFs), fascinating crystalline porous materials formed by a suitable combination of metal ions (nodes) with organic ligands (linkers), are promising platforms for a plethora of applications, spanning from fuel storage, CO_2 capture, catalysis to drug delivery, sensing and biomedicine. Indeed lanthanide-based MOFs (Ln–MOFs) have been attracting ever-growing interest in the last few decades because of their intrinsic advantages due to lanthanide coordination versatility and, depending on the lanthanide nature, the possibility to combine both luminescence and magnetic properties in the same crystal lattice, building up multifunctionality. Among magnetic Ln-MOFs, those exhibiting molecular properties, *i.e.* Single-Molecule Magnet (SMM) behavior, have attracted extensive attention for their potential applications in

cutting-edge molecular spintronics and quantum computing devices, since they allow for achieving in principle much higher densities with higher data processing speeds.[1–3] The most used Ln^{III} ions to construct SMMs are Tb^{III}, Dy^{III}, Er^{III} and Ho^{III} and particularly, Tb^{III} and Dy^{III} are the best candidates, since their electronic structures exhibit large magnetic anisotropy, due to the strong angular dependence of 4f orbitals.[4,5] Recently a second generation of SMM-based MOFs, known as Single Ion Magnet (SIM) MOFs, started to develop rapidly, since the first report of the $Ln(bipyNO)_4(TfO)_3$ (bipyNO = 4,40-bypyridyl-*N*,*N*0-dioxide, TfO = triflate) 3D coordination framework by Coronado, Mínguez Espallargas *et al.*[6] SIMs consist of single centres that exhibit slow magnetic relaxation[7] and, consequently, SIM-MOFs are formed by ordered assemblies of lanthanide ions and different bridging linkers, featuring extended and porous high-dimensional frameworks with tunable magnetic properties. The MOF framework is then used as a challenging scaffold to constrain or tune the local geometries of lanthanide nodes and arrange diverse organic linkers into ordered assemblies, featuring a combination of structural diversity and SMM/SIM behaviour. While a considerable effort has been made to enhance SIM performance, more detailed studies are still required to elucidate the origin of slow relaxation, as well as the influence of the ligand structure and crystal packing on SIM properties. According to the literature, highly symmetrical Dy^{III}-based SIMs, showing D_{4d}, D_{5h} and D_{6h} coordination geometries, providing reduced electron repulsion around the lanthanide ion and $m_J = \pm15/2$ state stabilization, prevent the quantum tunnel-

[a]*Instituto de Ciencia Molecular (ICMol), Universidad de Valencia, Catedrático José Beltrán 2, 46980 Paterna, Spain. E-mail: miguel.clemente@uv.es*
[b]*Dipartimento di Scienze Chimiche e Geologiche, Università degli Studi di Cagliari, Complesso Universitario di Monserrato, 09042 Monserrato, Italy.*
E-mail: mercuri@unica.it

†This article is dedicated to Prof. Enzo Cadoni for his retirement.
‡Electronic supplementary information (ESI) available: Elemental analysis, crystallographic tables and figures, PXRD patterns, IR spectra and tables and figures of magnetic characterization and modelling. CCDC 2320542–2320547. For ESI and crystallographic data in CIF or other electronic format see DOI: https://doi.org/10.1039/d4qi01549e
§Both authors contributed equally to this work.

This journal is © the Partner Organisations 2024

Inorg. Chem. Front., 2024, **11**, 5913–5923 | 5913

ling of magnetization (QTM).[8,9] Therefore, Ln-MOFs, possessing an approximately square-antiprismatic or dodecahedral coordination geometry, have the potential to exhibit SIM behavior. The magnetic relaxation behavior of these SIMs has been shown to be affected by the distortion of the coordination environment, generally due to subtle modifications of the crystal lattice that could be induced by the solvent, ancillary linkers and intermolecular interactions.[10–13] Therefore, the anisotropy of lanthanide ions and their magnetic dynamics are strongly influenced by both the ligand field and coordination geometry.[14] However, it is still a challenge to control the coordination geometry around the lanthanide ions in order to understand how it affects the relaxation mechanism. For this reason, shaping the geometries with properly designed organic linkers has become a successful strategy to achieve SIM-MOFs.

To design an extended coordination framework which exhibits SIM behavior, the choice of the organic linker and metal node is crucial. Most importantly the bridging ligand should be capable of constructing an extended framework and it should be a weak magnetic coupler, in order to keep Ln^{III} ions well isolated.[15] Among the linkers, the anilato derivatives *i.e.* 3,6-disubstituted-2,5-dihydroxy-1,4-benzoquinones have been successfully exploited as molecular building blocks for constructing Ln^{III}-based materials. Although these bridging ligands couple (antiferro)magnetically the transition metal nodes,[16,17] they provide a good magnetic isolation of Ln^{III} metal nodes as a result of the negligible overlap with their 4f orbitals.[15] Since the first report on Ln^{III}-based anilato complexes,[4] by Boskovic *et al.*, which consist of two Dy^{III}-based dimers, $[(Tp)_2Dy_2(Cl_2An)]\cdot 2CH_2Cl_2$ and $[(Tp)_2Dy_2((CH_3)_2An)]\cdot 1.1CH_2Cl_2$ (Tp^- = hydrotris(pyrazolyl) borate), showing slow relaxation of magnetization with Orbach and Raman relaxation mechanisms for $[(Tp)_2Dy_2(Cl_2An)]\cdot 2CH_2Cl_2$ (U_{eff} = 24 K) and a field induced SMM behavior and an Orbach mechanism for $[(Tp)_2Dy_2((CH_3)_2An)]\cdot 1.1CH_2Cl_2$ (U_{eff} = 47 K), several reports on complexes and 2D/3D anilato-based SMM/SIM CPs/MOFs have been thoroughly described in the literature.[15,18–20] Recently, the unexplored 3,6-*N*-ditriazolyl-2,5-dihydroxy-1,4-benzoquinone (H_2trz_2An), anilate,[21] has been used to construct 3D MOFs, due to the coordinative nitrogen of the triazole pendant arms of the anilato moiety.[17,22] Very recently, some of us reported on the synthesis and characterization of neutral polymorphic 3D frameworks, obtained by combining H_2trz_2An and NIR-emitting Er^{III} ions. These materials exhibit a combination of NIR emission and field-induced slow magnetic relaxation. Remarkably, one of the frameworks is a flexible MOF that undergoes a reversible structural phase transition, due to a dehydration/hydration process leading to pore shrinkage/expansion from a distorted hexagonal 2D to a 3,6-brickwall rectangular 3D structure. Remarkably its structural flexibility provokes a tuning of both luminescence and SIM properties with an improvement of magnetic blocking temperature.[23]

By reacting the same H_2trz_2An linker with Dy^{III}, Tb^{III} and Ho^{III} metal nodes, two different series are herein reported, formulated as $[Ln_2(trz_2An)_3(H_2O)_4]_n\cdot 10H_2O$ (Ln^{III} = Dy (**1a**), Tb (**2a**),

Ho (**3a**)) and $[Ln_2(trz_2An)_3(H_2O)_4]_n\cdot 7H_2O$ (Ln^{III} = Dy (**1b**), Tb (**2b**), Ho (**3b**)), which are isostructural with the Er^{III} frameworks and exhibit the same structural flexibility. All compounds were structurally and magnetically characterized, showing SIM behavior in the case of **1a**, **1b** and **2b**. Interestingly, the use of Tb^{III} in **2b** gave rise to the best SIM properties of this family of compounds. On the other hand, although the same structural flexibility in the porous frameworks was obtained for **1a**, it did not exhibit the drastic changes in SMM behavior induced by the dehydration observed previously for the Er^{III} derivative. The *ab initio* calculations support this behaviour, since **2b** shows less mixing between the m_J states of the ground state among all the studied coordination networks. Furthermore, they reveal that the change in the SMM behavior with dehydration relies on the nature of the electron density of the metal center and therefore the choice of the metal center plays a pivotal role in switching the SMM behavior.
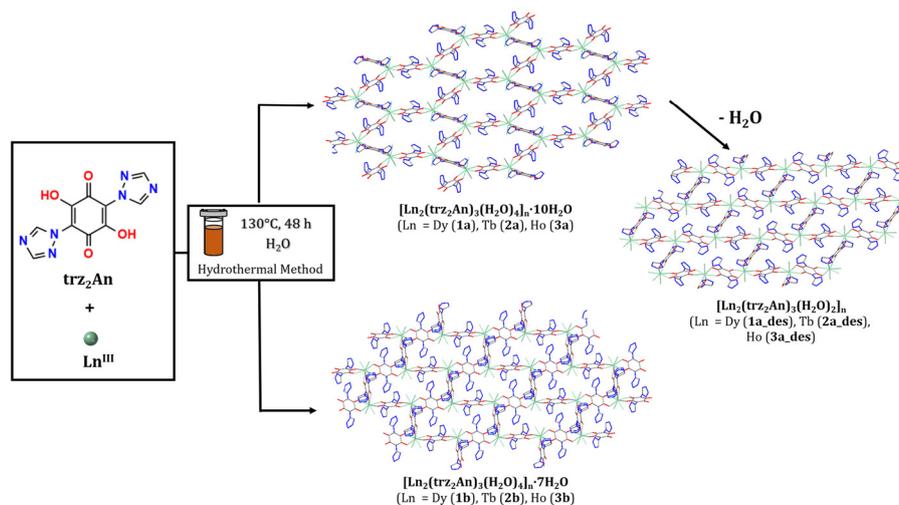
Results and discussion

Synthesis

Ln-based magnetic frameworks (**1–3a** and **1–3b**) were obtained by combining $Ln(NO_3)_3\cdot xH_2O$ with H_2trz_2An in a 1 : 1 ratio, *via* the hydrothermal method, following the same synthetic strategy reported for the preparation of Er^{III}-frameworks[23] (Scheme 1). As observed for Er^{III}, each batch gave two types of crystals which correspond to the two different phases previously reported and formulated as $[Ln_2(trz_2An)_3(H_2O)_4]_n\cdot 10H_2O$ (Ln^{III} = Dy (**1a**), Tb (**2a**), Ho (**3a**)), dark red block crystals, and $[Ln_2(trz_2An)_3(H_2O)_4]_n\cdot 7H_2O$ (Ln^{III} = Dy (**1b**), Tb (**2b**), Ho (**3b**)), orange prismatic crystals. To separate the crystals of the different phases the CH_2Cl_2/CH_2Br_2 solvent mixture in a 0.925/ 0.975 ratio was used. Interestingly **1–3a** MOFs show a reversible structural flexibility. With the removal of water solvent from phase **a**, by heating the samples at 80 °C or by applying vacuum, the reversible desolvated phase **a_des** formulated as $[Ln_2(trz_2An)_3(H_2O)_2]_n$ was afforded.

Crystal structures

Compounds **1–3a** and **1–3b** crystallize in the triclinic space group $P\bar{1}$. They are isostructural with the previously reported Er^{III} compounds.[23] Their structures were solved by single crystal X-ray diffraction (see Tables S2 to S9 in the ESI‡). They consist of 3D neutral coordination frameworks formed by Ln^{III} ions connected by trz_2An bridging linkers. The Ln^{III} ions are ennea-coordinated with a $\{NO_8\}$ coordination sphere arising from two oxygens of three bidentate trz_2An anilates, the N4 atom of one trz_2An and two coordinated water molecules (see figures in Tables S4 and S7 in the ESI‡). The Ln^{III} ions are linked to three neighboring ions through the oxygens of three trz_2An anilates, coordinating in bis-bidentate mode. This leads to layers with a (6,3) topology forming six-membered rings with distorted hexagonal cavities in **1–3a** and rectangular six-membered cavities, which adopt a brick-wall structure, in **1–3b** (see Scheme 1). Ln^{III} nodes of the same layer are connected to

5914 | *Inorg. Chem. Front.*, 2024, **11**, 5913–5923

This journal is © the Partner Organisations 2024

Scheme 1 Synthetic strategy for **1–3a**, **1–3a_des** and **1–3b**.

Ln^{III} nodes of other layers, through the N4 atom of the two pending triazolyl arms of one of the three trz_2An linkers.

Polycrystalline samples of **1a**, **2a** and **3a** were placed under vacuum in a Schlenk tube and then sealed in a glove box to study if vacuum could induce changes in the crystal structure. As observed with the Er^{III} compound, a reversible structural change was observed leading to new phases **1a_des**, **2a_des** and **3a_des** (Fig. 1). Furthermore, when **1a_des**, **2a_des** and **3a_des** were released in air, the samples were rehydrated forming again the **1a**, **2a** and **3a** phases as shown by PXRD measurements (Fig. 1). This proves that the dehydration/

hydration process is fully reversible, as well as the induced structural change. PXRD data suggest that the structures of **1–3a_des** are isostructural to the dehydrated compound obtained with Er^{III} of the formula $[Er_2(trz_2An)_3(H_2O)_2]_n \cdot 2H_2O$.

This rehydrated phase exhibits a drastic change from the distorted hexagonal 2D network found in **1a**, **2a** and **3a** to a distorted 3,6-brickwall rectangular structure related to the loss of one of the two coordination water molecules of the Ln^{III} ion, which shows, in these dehydrated compounds, a $\{NO_7\}$ coordination sphere arising from six oxygens of three bidentate trz_2An linkers, the N4 atom of one trz_2An linker and one coordinated water molecule.[23]
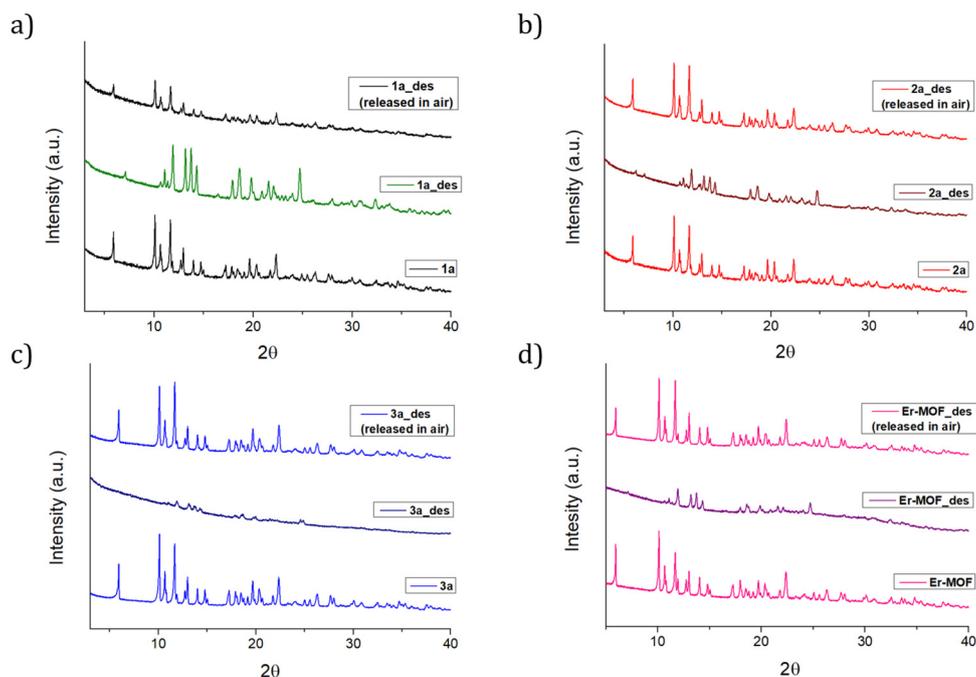

Fig. 1 PXRD experimental patterns of **1–3a**, **1–3a_des** and **1–3a_des** left in air 4 days after vacuum treatment, highlighting the complete reversibility of the structural change induced by dehydration. Panels *a*, *b* and *c* are for **1a**, **2a** and **3a**, respectively, while panel *d* shows the Er-MOF for comparison.

This structural change induces a decrease in the pore sizes. Thus, the distorted hexagonal cavities of **1–3a** compounds show maximum diagonal Ln^{III}–Ln^{III} distances of 22.1 Å and minimum Ln^{III}–Ln^{III} distances between atoms of opposite sides of 9.4 Å (**1a**), while the 3,6-brickwall rectangular structures of **1–3a_des** show the shortest Ln^{III}–Ln^{III} distances (maximum diagonal ones of 20.2 Å and minimum ones between atoms of opposite sides of 7.0 Å in the previously reported isostructural Er^{III} derivative[23]).

As previously demonstrated, the new phase **1–3a_des** can be obtained by dehydration under very mild conditions in a reversible way. Thus, the initial structure can be recovered by placing the dehydrated crystals in air, indicating a reversible structural phase transition between a hexagonal and a rectangular cavity, which has been already observed in other flexible MOFs.[24]

Magnetic properties

Solid state, dc magnetic susceptibility measurements were carried out in the temperature range of 2–300 K, under an applied magnetic field of 0.1 T, for **1–3a** and **1–3b**. As in Er^{III}-MOF, **phase a**, it was necessary to protect the sample with H_2O since the vacuum of the squid chamber ($\sim$2–3 mbar) caused desolvation and the formation of **1–3a_des**, even in the presence of eicosane. The $\chi_M T$ values at 300 K of 14.0 (**1a**), 13.9 (**1a_des**), 13.7 (**1b**), 11.7 (**2a**), 11.7 (**2a_des**), 11.3 (**2b**), 13.8 (**3a**), 13.8 (**3a_des**) and 13.7 (**3b**) cm³ K mol⁻¹, are in agreement with that expected for each non-interacting Ln^{III} ion ($^7F_6$ for Tb^{III}, $^6H_{15/2}$ for Dy^{III} and $^5I_8$ for Ho^{III}), as shown in Fig. 2–4 and S5–7, S9–11 and S13–15.‡ The field dependence of magnetization was also measured in the 2–8 K temperature range by varying the magnetic field up to 5 T (Fig. S17–S25‡). A sharp increase in magnetization was observed for Tb and Dy compounds at low magnetic fields but saturation was not observed at higher magnetic fields. On the other hand, the reduced magnetization curves at the different temperatures do not coincide (Fig. S17–25‡). These two facts suggest significant anisotropy. Finally, hysteresis of magnetization was not found in these compounds.

The dynamic magnetic properties were studied by susceptibility measurements performed with an alternating magnetic field (AC susceptibility). In the absence of a magnetic field, no signal in the out-of-phase molar susceptibility (χ'') was observed. When magnetic dc fields of 0.1 T were applied, strong frequency-dependent peaks in both the in-phase molar susceptibility (χ') and χ'' appeared in **1a**, **1a_des**, **1b** and **2b** with clear maxima of χ'' below 4 K for **1a** and **1a_des**, 6 K for **1b** and 14 K for **2b** (Fig. 5–8 and S26‡). This indicates that the four compounds present a field-induced slow relaxation of magnetization.

The χ' and χ'' peaks of **1a** measured in contact with eicosane (**1a_des**) present a small shift to higher temperatures of *ca.* 0.2 K with respect to those measured in contact with water **1a** (Fig. 8 and S26‡). This suggests that the magnetic behavior of **1a** is not as sensitive to desolvation as that of its correspondent Er^{III}-based MOF, as shown in Fig. 8.
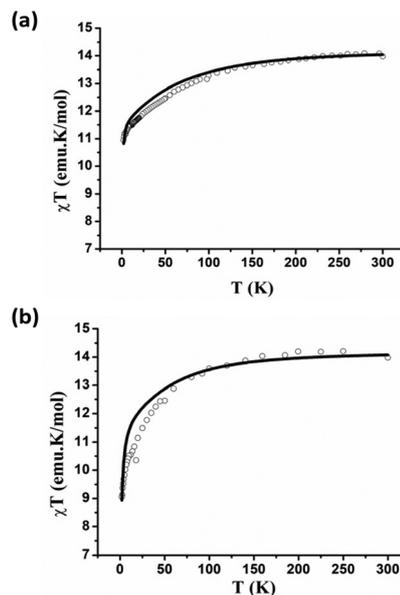

Fig. 2 Experimental (symbols) and predicted (solid line) temperature-dependence of $\chi_M T$ from 2 to 300 K, at 0.1 T of **1a_des** (a) and **1b** (b). We have added a TIP (temperature independent paramagnetism) value of 0.005 emu mol⁻¹ to correct the experimental χT value of **1a_des**. A dipolar coupling (z_J) of −0.02 and −0.08 cm⁻¹ was considered in our calculations for **1a_des** and **1b**, respectively, to simulate the experimental magnetic data. The z_J value is smaller in **1b** compared to that in **1a_des** due to the larger Dy···Dy distance in the former. The computed data have been scaled with a scaling factor of 0.9 and 1.1 for **1a_des** and **1b**, respectively.

To further investigate the observed magnetic behaviour of coordination networks **1–3** (both a and b) and the effect of dehydration in complex **1a**, we performed *ab initio* CASSCF/RASSI-SO/SINGLE_ANISO calculations using the MOLCAS 8.2 package.[25] Calculations were performed on a fragment of the MOF that contains one metal centre, keeping the coordination environment unchanged. The computed g factors of Kramers doublet 1 (KD1) ($g_{xx} = 0.140$, $g_{yy} = 0.244$, $g_{zz} = 18.777$ for **1a**, $g_{xx} = 0.002$, $g_{yy} = 0.006$, $g_{zz} = 19.328$ for **1a_des** and $g_{xx} = 0.021$, $g_{yy} = 0.041$, $g_{zz} = 19.547$ for **1b**) indicates a significant transverse magnetic anisotropy in all isomers of complex **1** (see Tables S11–S13‡) which explains the field induced SIM behaviour in these complexes. The magnetic anisotropy axis of KD1 in all these isomers is oriented along the –trz₂An ligand to minimize the electrostatic repulsion with the oblate electron density (see Fig. 9 and S6, S7‡). The ground KD is found to possess a dominant contribution from $m_J = |\pm 15/2\rangle$, whereas a significant mixing of $m_J = |\pm 13/2\rangle$ with other m_J states in the first excited KD leads to magnetization relaxation in **1a**, **1a_des** and **1b** *via* this KD (see Fig. 9 and S5–S7‡). This leads to the U_{cal} values of 71.6, 139.1 and 102.6 cm⁻¹ in **1a**, **1a_des** and **1b**, respectively. The computed magnetic susceptibility of the three derivatives is found to be in line with the experimental results (see Fig. 2 and S5–S7‡). We determined the relative donor strength by computing LoProp charges.[26] We can observe that removing one water molecule from the equatorial position of **1a** increases the axiality which is also reflected in

5916 | *Inorg. Chem. Front.*, 2024, **11**, 5913–5923

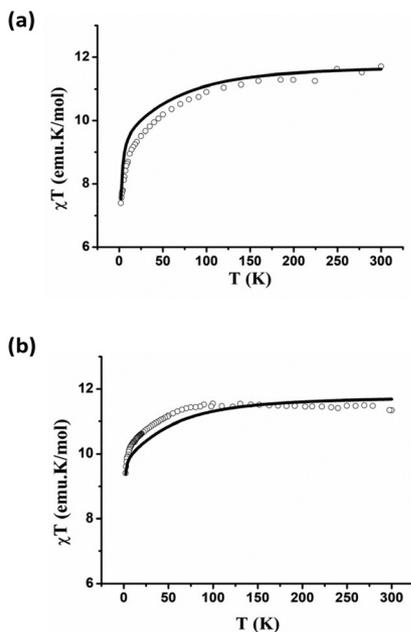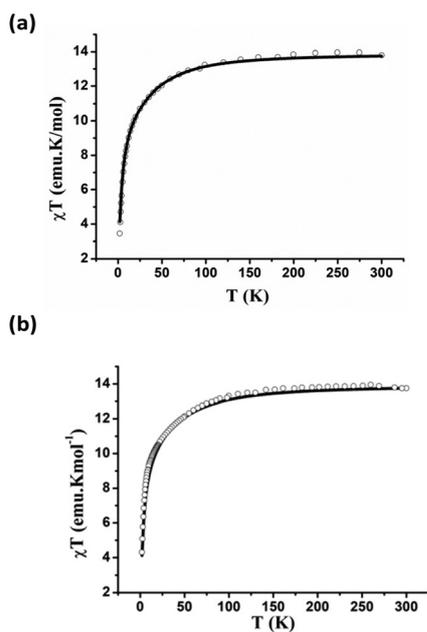This journal is © the Partner Organisations 2024

Fig. 3 Experimental (symbols) and predicted (solid line) temperature-dependence of $\chi_M T$ from 2 to 300 K, at 0.1 T of **2a_des** (a) and **2b** (b). We have added a TIP value of 0.005 emu mol^{-1} to correct the experimental χT value of **2a_des**. We have added a scaling factor of 0.9 to correct the experimental χT value of **2b**. A dipolar coupling (z_J) of -0.05 and -0.01 cm^{-1} was considered in our calculations for **2a_des** and **2b**, respectively, to simulate the experimental magnetic data.

Fig. 4 Experimental (symbols) and predicted (solid line) temperature-dependence of $\chi_M T$ from 2 to 300 K, at 0.1 T of **3a_des** (a) and **3b** (b). The experimental data have been scaled by a factor of 0.8 for **3a_des**. A dipolar coupling (z_J) of -0.5 and -0.4 cm^{-1} was considered in our calculations for **3a_des** and **3b**, respectively, to simulate the experimental magnetic data.
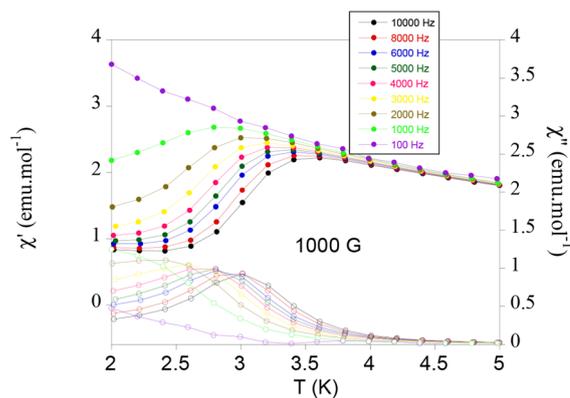

Fig. 5 Temperature dependence of χ' (full symbols) and χ'' (empty symbols) of **1a_des** in an applied dc field of 0.1 T at frequencies in the range 100 to 10 000 Hz.
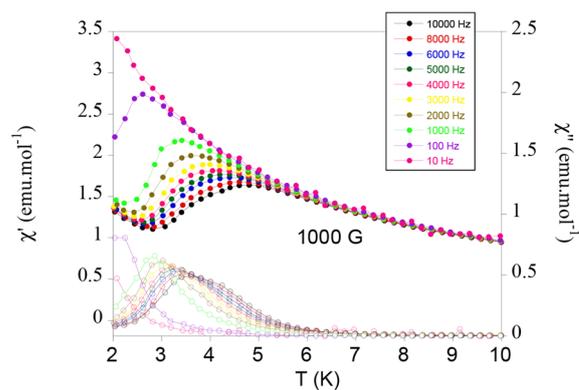

Fig. 6 Temperature dependence of χ' (full symbols) and χ'' (empty symbols) of **1b** in an applied dc field of 0.1 T at frequencies in the range 10 to 10 000 Hz.
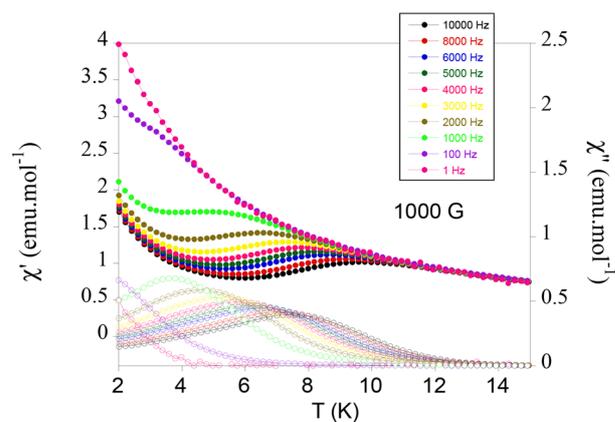

Fig. 7 Temperature dependence of χ' (full symbols) and χ'' (empty symbols) of **2b** in an applied dc field of 0.1 T at frequencies in the range 1 to 10 000 Hz.

This journal is © the Partner Organisations 2024

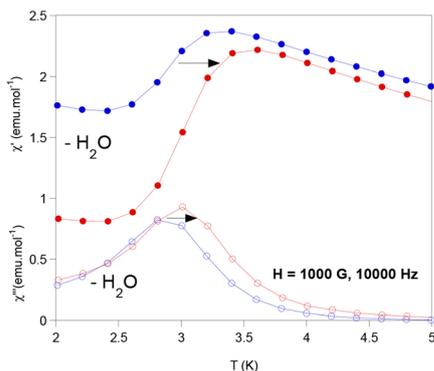*Inorg. Chem. Front.*, 2024, **11**, 5913–5923 | **5917**

Fig. 8 Temperature dependence of χ' and χ'' of **1a** (full and empty blue circles, respectively) and **1a_des** (full and empty red circles, respectively) in an applied dc field of 0.1 T at 10 000 Hz.
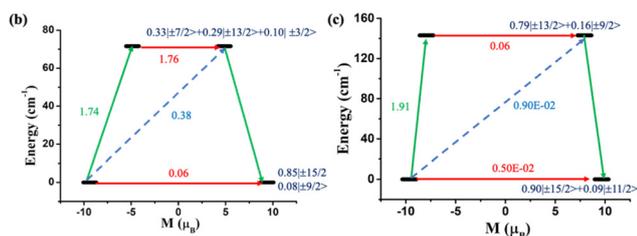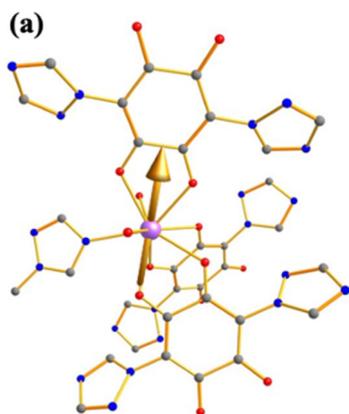

Fig. 9 (a) The anisotropy axis of KD1 of **1a**. Colour code: Dy: purple, O: red, N: blue, and C: grey. Hydrogens are omitted for clarity. The mechanism of magnetization relaxation of (b) **1a** and (c) **1a_des**. The red arrow represents QTM *via* the ground state and TA-QTM *via* first excited state. The sky blue dotted arrow represents the Orbach process. The green arrow shows the possible mechanism of magnetization relaxation.

the slight increase of the LoProp charge of the coordinated atoms at the axial position (see Table S14 and Fig. S8‡). Therefore, it quenches the quantum tunneling of magnetization (QTM) and increases the U_{cal} value in **1a_des** compared to that in **1a**. This is also in agreement with the experimental result where improvement in magnetic properties is observed in **1a_des** compared to those in **1a**. In comparison with the Er analogue, the change in magnetic properties from **1a** to **1a_des** is not drastic. This can be ascribed to the nature of electron density, the $m_J = |\pm 15/2\rangle$ oblate in nature in Dy(III) while being

prolate in Er^{III}. The removal of the water molecule from the equatorial position strongly affects the electronic structure of Er(III) compared to that of Dy(III). Furthermore, the increment of U_{cal} and quenching of QTM from **1a** to **1b** can be again explained by analysing the LoProp charge of the equatorial atoms, which decreases, whereas in the axial atoms it increases (see Table S14 and Fig. S8‡). Then, we computed the crystal field parameters (CFPs) using Stevens Hamiltonian,

$$\hat{H}_{CF} = \sum_{k=2,4,6} \sum_{q=-k}^{+k} B_k^q \tilde{O}_k^q,$$ where B_k^q represents the CFPs and $\tilde{O}_k^q$ represents the Stevens operator.[26] The negative value of the B_2^0 crystal field parameter explains strong axiality in all the coordination networks (see Table S15‡) and the value of B_2^0 increases from **1a** to **1a_des**, which agrees well with the increase of axiality after dehydration of **1a** (Table S15‡). To explain the relaxation of magnetization, molecular vibrations also play a key role.[27] In this regard, the octacoordinated system presents less active vibrations due to the loss of a water molecule. However, the actual effect will depend on the level of resonance of those molecular vibrations with the electronic energy levels.

Subsequently, we computed the electronic and magnetic properties of coordination networks **2a**, **2a_des** and **2b**. The calculations reveal significant tunnel splitting (V_{tun}) in the ground pseudo-Kramers doublet (pKD) of **2a** while a negligible V_{tun} is observed in **2a_des** and **2b** (see Tables S16 and 17 in the ESI‡). The strong V_{tun} in **2a** is correlated with the larger and smaller LoProp charges in the equatorial coordinated atoms compared to that in **2b** (see Fig. S12 and Table S18‡), which is also reflected in the computed CF parameters (Table S19‡). This explains the absence and presence of SMM behavior in **2a** and **2b**, respectively. The computed magnetic susceptibility in all the isomers of **2** are found to be in good agreement with the experimental result (Fig. 3 and S9–11‡). However, the strong V_{tun} in the first excited pKD of **2b** reinforces the relaxation of the magnetization, leading to $U_{cal} = 141$ cm^{-1} (see Fig. S11‡). This value of U_{cal} is largely overestimated compared to that of U_{eff}, which can be ascribed to the metal–ligand covalency, dipolar coupling and dynamic correlation that have not been included in our calculations. Compared to **1a**, **1a_des** and **1b**, the compound **2b** shows less mixing among m_J states. This results in effective quenching of V_{tun}, and therefore, it displays the best SMM characteristics among all the coordination networks studied here.

Finally, to investigate the possibility of SMM behavior, we extended our simulations to coordination networks **3a**, **3a_des** and **3b**. Although the computed magnetic susceptibility of all coordination networks is found to be in good agreement with the experimental result (Fig. 4 and S13–15‡), the ground pKDs possess strong m_J mixing that yields significant V_{tun}, which explains the absence of SMM behavior in these coordination networks (Tables S20–23‡).

Between, **3a**, **3a_des** and **3b**, a smaller V_{tun} is observed in **3a** due to smaller equatorial and larger axial LoProp charges of the coordinated atoms compared to **3a_des** and **3b** (Fig. S16 and Table S22‡), which is also reflected in the computed CF parameters (Table S23‡).

5918 | *Inorg. Chem. Front.*, 2024, **11**, 5913–5923

This journal is © the Partner Organisations 2024

The relaxation times (τ) of **1a_des**, **1b** and **2b** were determined from the maximum of χ'' at a given frequency ($\tau = 1/2\pi\nu$) and from the Debye model. They were fitted to the Arrhenius expression for a thermally activated process (Orbach, $\tau = \tau_0 \exp (U_{\mathrm{eff}}/k_B T)$) leading to $\tau_0 = 5.4 \times 10^{-8}$ s and $U_{\mathrm{eff}} = 17.5$ K for **1a_des**, $\tau_0 = 1.2 \times 10^{-8}$ s and $U_{\mathrm{eff}} = 25.7$ K for **1b**, and $\tau_0 = 2.0 \times 10^{-6}$ s and $U_{\mathrm{eff}} = 16.4$ K at 0.1 T for **2b**. However, the plots of τ vs. $1/T$ deviate from linearity at low temperatures for **1a_des** and **2b** indicating the coexistence of multiple relaxation pathways as observed in the Er^{III} frameworks previously reported[23] and other anilate-based lanthanide coordination networks (see Fig. S27‡). The general model where the first, second, third and fourth terms include quantum tunneling, direct, Raman and Orbach relaxation processes, respectively, was applied.

$$\tau^{-1} = \tau_{\mathrm{QTM}}^{-1} + AH^2T + CT^n + \tau_0^{-1} \exp(-U_{\mathrm{eff}}/K_B T)$$

Correct fitting of **2b** was obtained using Raman and Orbach relaxation processes with values comparable to those found for other anilate-based Ln^{III} compounds with $C = 81.7$ s^{-1} K$^{-3.2}$, $\tau_0 = 1.0 \ 10^{-6}$ s and $U_{\mathrm{eff}} = 30.5$ K.[28–31] The calculated value of n (3.2) is smaller than the ideal value of 9 found for Raman processes. This suggests that these Raman-like relaxations are attributed to acoustic and optical vibrations.[32] In the case of **1a_des**, a reasonable fitting using Raman and Orbach relaxation processes could not be obtained. This was obtained by combining direct and Orbach relaxation processes with $AH^2 = 3541.7$ s^{-1}, $\tau_0 = 3.5 \ 10^{-10}$ s and $U_{\mathrm{eff}} = 32.8$ K (Fig. S28‡).

The variable-frequency AC data at different temperatures of **1a_des**, **1b** and **2b** show a single relaxation with maxima at 960 Hz (**1a_des**), 65 Hz (**1b**) and 210 Hz (**2b**) at 2 K (see Fig. S30–33‡). The Cole–Cole plots (χ'' vs. χ') of the three samples confirm the presence of a single relaxation process (Fig. S29‡). Thus, at fixed temperatures between 2.0 and 5.0 K for **1a_des**, 2.0 and 4.0 for **1b** and 2.0 and 7.5 K for **2b**, semicircular plots were obtained and fitted using a generalized Debye model, yielding an α parameter in the ranges of 0.12–0.42 (**1a_des**), 0.21–0.25 (**1b**) and 0.06–0.33 (**2b**). This indicates narrow distributions of the relaxation processes.

Conclusions

The H$_2$trz$_2$An anilate derivative, bearing a triazole pendant arm at the 3,6 position of the anilato *core*, has been used for the first time in combination with Dy^{III}, Tb^{III} and Ho^{III} nodes to afford **1–3a** and **1–3b** 3D frameworks, formed by 2D layers with a (6,3) topology, connected through the triazolyl pendant groups of the anilato linkers. These compounds are isostructural to the previously reported Er^{III} frameworks.[23] Remarkably, **1–3a** are MOFs showing flexibility as the Er^{III}-MOF (phase **a**), with analogous reversible drastic structural changes to a less porous 3D structure, after partial dehydration under very mild conditions. The use of these three metals enables optimization of the SIM properties. Magnetic characterization reveals a field-induced SIM behaviour for **1a, 1a_des**

and **1b** Dy^{III} compounds and for the **2b** Tb^{III} compound, which, to the best of our knowledge, is the first Tb^{III}–anilate-based coordination polymer that exhibits SIM behaviour. Conversely, the SIM properties of **1a** are much less sensitive to the removal of water molecules than those of the previously reported Er^{III}-MOF. Interestingly, the blocking temperature of the Tb^{III} compound is higher than those of Er^{III} and Dy^{III} compounds, showing the best SIM properties within this series. Remarkably theoretical calculations evidenced that **2b**, compared to **1a**, **1a_des** and **1b**, shows less mixing among m_J states, resulting in effective quenching of V_{tun}, and therefore the best SIM properties among all coordination networks herein studied. Furthermore, they reveal that the choice of the metal center plays a crucial role in switching the SMM behavior, since the dehydration process depends on the electron density nature of the metal center. Finally, retention of the flexibility and porosity of this family of compounds with different lanthanide ions paves the way for the preparation of other members of this family of coordination polymers/MOFs with other NIR emitting metal ions such as Nd^{III} and Yb^{III}, which could allow a fine tuning of other properties such as luminescence by the reversible dehydration/rehydration process. Further optimization of SIM properties could also be achieved by diluting the paramagnetic Tb^{III} nodes with diamagnetic ions such as Eu^{III}.

Experimental section

General remarks

The lanthanide precursors, NaOH in pellets and the solvents used were purchased from AlfaAesar and Exacta Optech and used without further purification. The synthesis of the ligand H$_2$trz$_2$An was performed as reported in the literature.[21] Elemental analyses (C, H, and N) were performed with a CE Instruments EA 1110 CHNS. FT-IR spectra were collected using a Bruker Equinox 55 spectrometer on KBr pellets.

Synthesis of [Ln$_2$(trz$_2$An)$_3$(H$_2$O)$_4$]$_n$·10H$_2$O (Ln^{III} = Dy (1a), Tb (2a), Ho (3a)) and [Ln$_2$(trz$_2$An)$_3$(H$_2$O)$_4$]$_n$·7H$_2$O (Ln^{III} = Dy (1b), Tb (2b), Ho (3b))

These series were prepared by using the same synthetic procedure for Er^{III} compounds.[23] A 5 mL Teflon vial with a mixture of Ln(NO$_3$)$_3$·6H$_2$O (0.05 mmol; 17.4 mg (**1**), 22.6 mg (**2**), 18.9 mg (**3**)), H$_2$trz$_2$An (0.05 mmol, 13.7 mg), NaOH (0.1 mmol, 4 mg) and water (5 mL) was heated at 130 °C for 48 hours and then the vial was slowly cooled to room temperature. The heating and cooling rates were 0.92 K min^{-1} and 0.15 K min^{-1}, respectively. Two different types of crystals were obtained from the same batch, dark red-block crystals (phase **a**) and orange prismatic crystals (phase **b**), both of them suitable for single-crystal X-ray diffraction measurements. Their density's difference was exploited to separate them, using a CH$_2$Cl$_2$/CH$_2$Br$_2$ solvent mixture in a ratio of 0.925/0.975 as reported for the Er^{III} frameworks. Elemental analysis is reported in Table S1.‡ The results from elemental analysis

suggest the absorption of one (phase **a**) and three (phase **b**) water molecules after filtering.

Synthesis of $[Ln_2(trz_2An)_3(H_2O)_2]_n$ (Ln = Dy (1a_des), Tb (2a_des), Ho (3a_des))

Polycrystalline powders of **1–3a** were placed under vacuum in a vacuum line pump and then sealed in a glove box to obtain the dehydrated phase **a_des**. Elemental analysis of **1a_des** is not shown since it turns to the structure of **1a** after two days in air.

X-Ray crystallography

Single crystal X-ray diffraction was performed on **1–3a** and **1–3b** crystals, which were mounted on a glass fiber using a viscous hydrocarbon oil to coat the single crystal and then transferred directly to the cold nitrogen stream for data collection. X ray data were collected at 120 K for all the samples. Measurements were performed on a Supernova diffractometer equipped with a graphite-monochromated Enhance (Mo) X-ray source (λ = 0.710 73 Å). The program CrysAlisPro, Oxford Diffraction Ltd, was used for unit cell determination and data reduction. Empirical absorption correction was performed using spherical harmonics, implemented in the SCALE3 ABSPACK scaling algorithm. The structures were solved with the ShelXT structure solution program[33] and refined with the SHELXL-2013 program,[34] using Olex2.[35] Non-hydrogen atoms were refined anisotropically, and hydrogen atoms were placed at calculated positions refined using idealized geometries (riding model) and assigned fixed isotropic displacement parameters. Crystallographic data of all the compounds are summarized in Tables S2 and S3.‡ CCDC 2320542–2320547‡ contain the supplementary crystallographic data for this paper.

All powder X-ray diffraction patterns (PXRD) were obtained using a 0.7 mm glass capillary filled with polycrystalline samples of the compounds and mounted and aligned on an Empyrean PANalytical powder diffractometer, using Cu Kα radiation (λ = 1.541 77 Å). A total of three scans were collected for each compound at room temperature in the 2θ range of 5–40°. Polycrystalline samples of **1–3a** were further placed under vacuum in a vacuum line pump and were then opened in the glove box to be sealed in the 0.7 mm glass capillary.

Magnetic measurements

Magnetic measurements were performed with Quantum Design MPMS-XL-5 SQUID and PPMS-9 magnetometers in the 2–300 K temperature range with an applied magnetic field of 0.1 T at a scan rate of 2 K min^{-1}. In the case of **1–3a**, it was necessary to protect the sample covering it with H_2O since the vacuum of the squid chamber caused desolvation and the formation of **1–3a_des**.

Theoretical calculations

The optimization of the hydrogen positions of the chosen molecular fragment (except **2a**, **2a_des** and **2b**) was performed using the hybrid B3LYP exchange–correlation functional[36] (with Grimme-D3 dispersion corrections) with the Gaussian 09 programme package.[37] During the optimization, the Dy(III) ion was replaced with diamagnetic Y(III) to facilitate smooth SCF convergence.[38] We have employed the Ahlrichs triple-ζ valence plus polarization basis set for oxygen and nitrogen and the 6-31G* basis set for carbon and hydrogen.[39] For Y(III), Stuttgart's effective core potential (SDD ECP, 28 core electrons) was used with its corresponding basis set.[40,41] A quadratic convergence method was employed in all our calculations.[42]

All the *ab initio* CASSCF/RASSI-SO/SINGLE_ANISO calculations have been performed using the MOLCAS 8.2 programme package considering a fragment of the MOF with only one metal centre.[25] We have used Douglas–Kroll–Hess Hamiltonian to take into account the relativistic effect.[43] The disk space of our calculations has been reduced using the Cholesky decomposition technique. All the basis sets employed in our calculations have been taken from the ANO-RCC library implemented in the MOLCAS 8.2 programme package.[44,45] We have used the [Dy.ANO-RCC···8s7p5d3f2g1 h.] basis set for Dy, [Tb.ANO-RCC···8s7p5d3f2g1 h.] basis set for Tb, [O.ANO-RCC···3s2p1d.] basis set for O, [N.ANO-RCC···3s2p1d.] basis set for N, [C.ANO-RCC···3s2p.] basis set for C and [H.ANO-RCC···2s.] basis set for H in our calculations. The CAS(8,7), CAS(9,7) and CAS(10,7) active spaces were employed for Tb^{III}, Dy^{III} and Ho^{III}, respectively, in our calculations taking into account all the valence electrons of Dy^{III} in seven 4f orbitals. We have used only 21 sextets for Dy^{III} as this has been able to reproduce the experimental observables from the previous studies. We have also computed the energies of 7 septets, 140 quintets and 195 triplets for Tb^{III} and 35 quintets, 210 triplets and 196 singlets for Ho^{III} from the CASSCF calculations. The spin-free states (7 septets, 105 quintets and 112 triplets for Tb^{III} and 35 quintets, 117 triplets and 75 singlets for Ho^{III}) have been mixed using RASSI-SO[46] to generate spin orbit coupled states. Finally, the g tensor, blocking barrier, QTM *etc*. have been extracted from the SINGLE_ANISO module of MOLCAS 8.2.

Author contributions

MLM and NM designed the compounds. MLM and MCL supervised the research project. NM synthesized and characterized the compounds under the supervision of MLM, EC and MCL (structural and magnetic characterization) and with the help of VGL and MO. JJB and SD performed the theoretical calculations and analyzed the magnetic data. MLM, MCL and SD wrote the manuscript. All authors contributed to the final interpretation of the experimental results and critically revised the manuscript. All authors have read and approved the final version of the manuscript.

Data availability

The data supporting this article have been included as part of the ESI.‡

5920 | *Inorg. Chem. Front.*, 2024, **11**, 5913–5923

This journal is © the Partner Organisations 2024

Crystallographic data have been deposited at the CCDC under CCDC 2320542–2320547‡ and can be obtained from https://doi.org/10.1039/x0xx00000x.

Conflicts of interest

There are no conflicts to declare.

Acknowledgements

References

1 M. N. Leuenberger and D. Loss, Quantum computing in molecular magnets, *Nature*, 2001, **410**, 789–793.

2 A. Ardavan, O. Rival, J. J. L. Morton, S. J. Blundell, A. M. Tyryshkin, G. A. Timco and R. E. P. Winpenny, Will Spin-Relaxation Times in Molecular Magnets Permit Quantum Information Processing?, *Phys. Rev. Lett.*, 2007, **98**, 1–4.

3 D. N. Woodruff, R. E. P. Winpenny and R. A. Layfield, Lanthanide Single-Molecule Magnets, *Chem. Rev.*, 2013, **113**, 5110–5148.

4 M. A. Dunstan, E. Rousset, M. E. Boulon, R. W. Gable, L. Sorace and C. Boskovic, Slow magnetisation relaxation in tetraoxolene-bridged rare earth complexes, *Dalton Trans.*, 2017, **46**, 13756–13767.

5 F. Gendron, B. Pritchard, H. Bolvin and J. Autschbach, Single-ion 4f element magnetism: an *ab initio* look at Ln $(COT)_2^-$, *Dalton Trans.*, 2015, **44**, 19886–19900.

6 J. J. Baldoví, E. Coronado, A. Gaita-Ariño, C. Gamer, M. Giménez-Marqués and G. Mínguez Espallargas, A SIM-MOF: three-dimensional organisation of single-ion magnets with anion-exchange capabilities, *Chem. – Eur. J.*, 2014, **20**, 10695–10702.

7 B. Fernández, I. Oyarzabal, E. Fischer-Fodor, S. MacAvei, I. Sánchez, J. M. Seco, S. Gómez-Ruiz and A. Rodríguez-Diéguez, Multifunctional applications of a dysprosium-based metal–organic chain with single-ion magnet behaviour, *CrystEngComm*, 2016, **18**, 8718–8721.

8 H. Wu, M. Li, Z. Xia, V. Montigaud, O. Cador, B. Le Guennic, H. Ke, W. Wang, G. Xie, S. Chen and S. Gao, High temperature quantum tunnelling of magnetization and thousand kelvin anisotropy barrier in a Dy_2 single-molecule magnet, *Chem. Commun.*, 2021, **57**, 371–374.

9 P. H. Lin, T. J. Burchell, R. Clérac and M. Murugesu, Dinuclear Dysprosium(III) Single-Molecule Magnets with a Large Anisotropic Barrier, *Angew. Chem., Int. Ed.*, 2008, **47**, 8848–8851.

10 K. Liu, H. Li, X. Zhang, W. Shi and P. Cheng, Constraining and Tuning the Coordination Geometry of a Lanthanide Ion in Metal-Organic Frameworks: Approach toward a Single-Molecule Magnet, *Inorg. Chem.*, 2015, **54**, 10224–10231.

11 Y. Xin, J. Wang, M. Zychowicz, J. J. Zakrzewski, K. Nakabayashi, B. Sieklucka, S. Chorazy and S. I. Ohkoshi, Dehydration–Hydration Switching of Single-Molecule Magnet Behavior and Visible Photoluminescence in a Cyanido-Bridged DyIIICoIII Framework, *J. Am. Chem. Soc.*, 2019, **141**, 18211–18220.

12 U. Huizi-Rayo, A. Zabala-Lekuona, A. Terenzi, C. M. Cruz, J. M. Cuerva, A. Rodríguez-Diéguez, J. A. García, J. M. Seco, E. San Sebastian and J. Cepeda, Influence of thermally induced structural transformations on the magnetic and luminescence properties of tartrate-based chiral lanthanide organic-frameworks, *J. Mater. Chem. C*, 2020, **8**, 8243–8256.

13 S. Benmansour, C. Pintado-Zaldo, J. Martínez-Ponce, A. Hernández-Paredes, A. Valero-Martínez, M. Gómez-Benmansour and C. J. Gómez-García, The Versatility of Ethylene Glycol to Tune the Dimensionality and Magnetic Properties in DyIII-Anilato-Based Single-Ion Magnets, *Cryst. Growth Des.*, 2023, **23**, 1269–1280.

14 F. Manna, M. Oggianu, N. Avarvari and M. L. Mercuri, Lanthanide-Based Metal–Organic Frameworks with Single-Molecule Magnet Properties, *Magnetochemistry*, 2023, **9**, 190.

15 S. Benmansour and C. J. Gómez-García, Lanthanoid-Anilato Complexes and Lattices, *Magnetochemistry*, 2020, **6**, 1–44.

16 S. Kawata, S. Kitagawa, H. Kumagai, T. Ishiyama, K. Honda, H. Tobita, K. Adachi and M. Katada, Novel intercalation host system based on transition metal (Fe^{2+}, Co^{2+}, Mn^{2+})-chloranilate coordination polymers. Single crystal structures and properties, *Chem. Mater.*, 1998, **10**, 3902–3912.

17 N. Monni, E. Andres-Garcia, K. Caamaño, V. García-López, J. M. Clemente-Juan, M. Giménez-Marqués, M. Oggianu, E. Cadoni, G. Mínguez Espallargas, M. Clemente-León, M. L. Mercuri and E. Coronado, A thermally/chemically robust and easily regenerable anilato-based ultramicropor-

This journal is © the Partner Organisations 2024

Inorg. Chem. Front., 2024, **11**, 5913–5923 | **5921**

ous 3D MOF for CO_2 uptake and separation, *J. Mater. Chem. A*, 2021, **9**, 25189–25195.

18   S. Benmansour, A. Hernández-Paredes, M. Bayona-Andrés and C. J. Gómez-García, Slow Relaxation of the Magnetization in Anilato-Based Dy(III) 2D Lattices, *Molecules*, 2021, **26**, 1–21.

19   S. Benmansour, C. J. Gómez-García and A. Hernández-Paredes, The Complete Series of Lanthanoid-Chloranilato Lattices with Dimethylsulfoxide: Role of the Lanthanoid Size on the Coordination Number and Crystal Structure, *Crystals*, 2022, **12**, 261.

20   H. Q. Li, G. L. Wang, Y. C. Sun, Y. Q. Zhang and X. Y. Wang, Solvent Modification of the Structures and Magnetic Properties of a Series of Dysprosium(III) Single-Molecule Magnets, *Inorg. Chem.*, 2022, **61**, 17537–17549.

21   W. Gauβ, H. Heitzer and S. Petersen, Umsetzungen von Chinonen mit stickstoffhaltigen Heteroaromaten, *Justus Liebigs Ann. Chem.*, 1973, **764**, 131–144.

22   C. J. Kingsbury, B. F. Abrahams and R. Robson, CCDC 1568063, *Exp. Cryst. Struct. Determ.*, 2017, DOI: **10.5517/ccdc.csd.cc1pmppp**.

23   N. Monni, J. J. Baldoví, V. García-López, M. Oggianu, E. Cadoni, F. Quochi, M. Clemente-León, M. L. Mercuri and E. Coronado, Reversible tuning of luminescence and magnetism in a structurally flexible erbium–anilato MOF, *Chem. Sci.*, 2022, **13**, 7419–7428.

24   M. Souto, J. Romero, J. Calbo, I. J. Vitórica-Yrezábal, J. L. Zafra, J. Casado, E. Ortí, A. Walsh and G. Mínguez Espallargas, Breathing-Dependent Redox Activity in a Tetrathiafulvalene-Based Metal–Organic Framework, *J. Am. Chem. Soc.*, 2018, **140**, 10562–10569.

25   I. Fdez Galván, M. Vacher, A. Alavi, C. Angeli, F. Aquilante, J. Autschbach, J. J. Bao, S. I. Bokarev, N. A. Bogdanov, R. K. Carlson, L. F. Chibotaru, J. Creutzberg, N. Dattani, M. G. Delcey, S. S. Dong, A. Dreuw, L. Freitag, L. M. Frutos, L. Gagliardi, F. Gendron, A. Giussani, L. González, G. Grell, M. Guo, C. E. Hoyer, M. Johansson, S. Keller, S. Knecht, G. Kovačević, E. Källman, G. Li Manni, M. Lundberg, Y. Ma, S. Mai, J. P. Malhado, P. Å. Malmqvist, P. Marquetand, S. A. Mewes, J. Norell, M. Olivucci, M. Oppel, Q. M. Phung, K. Pierloot, F. Plasser, M. Reiher, A. M. Sand, I. Schapiro, P. Sharma, C. J. Stein, L. K. Sørensen, D. G. Truhlar, M. Ugandi, L. Ungur, A. Valentini, S. Vancoillie, V. Veryazov, O. Weser, T. A. Wesołowski, P. O. Widmark, S. Wouters, A. Zech, J. P. Zobel and R. Lindh, OpenMolcas: From source code to insight, *J. Chem. Theory Comput.*, 2019, **15**, 5925–5964.

26   L. F. Chibotaru and L. Ungur, Ab initio calculation of anisotropic magnetic properties of complexes. I. Unique definition of pseudospin Hamiltonians and their derivation, *J. Chem. Phys.*, 2012, **137**, 064112.

27   L. Escalera-Moreno, J. J. Baldoví, A. Gaita-Ariño and E. Coronado, Spin states, vibrations and spin relaxation in molecular nanomagnets and spin qubits: a critical perspective, *Chem. Sci.*, 2018, **9**, 3265–3275.

28   S. Benmansour, A. Hernández-Paredes, A. Mondal, G. López Martínez, J. Canet-Ferrer, S. Konar and C. J. Gómez-García, Slow relaxation of the magnetization, reversible solvent exchange and luminescence in 2D anilato-based frameworks, *Chem. Commun.*, 2020, **56**, 9862–9865.

29   A. Mondal, S. Roy and S. Konar, Remarkable Energy Barrier for Magnetization Reversal in 3D and 2D Dysprosium-Chloranilate-Based Coordination Polymers, *Chem. – Eur. J.*, 2020, **26**, 8774–8783.

30   P. Zhang, M. Perfetti, M. Kern, P. P. Hallmen, L. Ungur, S. Lenz, M. R. Ringenberg, W. Frey, H. Stoll, G. Rauhut and J. Van Slageren, Exchange coupling and single molecule magnetism in redox-active tetraoxolene-bridged dilanthanide complexes, *Chem. Sci.*, 2018, **9**, 1221–1230.

31   W. R. Reed, M. A. Dunstan, R. W. Gable, W. Phonsri, K. S. Murray, R. A. Mole and C. Boskovic, Tetraoxolene-bridged rare-earth complexes: a radical-bridged dinuclear Dy single-molecule magnet, *Dalton Trans.*, 2019, **48**, 15635–15645.

32   R. Ishikawa, S. Michiwaki, T. Noda, K. Katoh, M. Yamashita and S. Kawata, Series of Chloranilate-Bridged Dinuclear Lanthanide Complexes: Kramers Systems Showing Field-Induced Slow Magnetic Relaxation, *Magnetochemistry*, 2019, **5**, 30–42.

33   G. M. Sheldrick, SHELXT – Integrated space-group and crystal-structure determination, *Acta Crystallogr., Sect. A: Found. Adv.*, 2015, **71**, 3–8.

34   G. M. Sheldrick, Crystal structure refinement with SHELXL, *Acta Crystallogr., Sect. C: Struct. Chem.*, 2015, **71**, 3–8.

35   O. V. Dolomanov, L. J. Bourhis, R. J. Gildea, J. A. K. Howard and H. Puschmann, OLEX2: a complete structure solution, refinement and analysis program, *J. Appl. Crystallogr.*, 2009, **42**, 339–341.

36   A. D. Becke, A new mixing of Hartree–Fock and local density–functional theories, *J. Chem. Phys.*, 1993, **98**, 1372–1377.

37   M. J. Frisch, G. W. Trucks, H. B. Schlegel, G. E. Scuseria, M. A. Robb, J. R. Cheeseman, G. Scalmani, V. Barone, B. Mennucci, G. A. Petersson, H. Nakatsuji, M. Caricato, X. Li, H. P. Hratchian, A. F. Izmaylov, J. Bloino, G. Zheng, J. L. Sonnenberg, M. Hada, M. Ehara, K. Toyota, R. Fukuda, J. Hasegawa, M. Ishida, T. Nakajima, Y. Honda, O. Kitao, H. Nakai, T. Vreven, J. A. Montgomery, J. E. Peralta, F. Ogliaro, M. Bearpark, J. J. Heyd, E. Brothers, K. N. Kudin, V. N. Staroverov, R. Kobayashi, J. Normand, K. Raghavachari, A. Rendell, J. C. Burant, S. S. Iyengar, J. Tomasi, M. Cossi, N. Rega, J. M. Millam, M. Klene, J. E. Knox, J. B. Cross, V. Bakken, C. Adamo, J. Jaramillo, R. Gomperts, R. E. Stratmann, O. Yazyev, A. J. Austin, R. Cammi, C. Pomelli, J. W. Ochterski, R. L. Martin, K. Morokuma, V. G. Zakrzewski, G. A. Voth, P. Salvador, J. J. Dannenberg, S. Dapprich, A. D. Daniels, O. Farkas, J. B. Foresman, J. V. Ortiz, J. Cioslowski and D. J. Fox, *Gaussian 09, Revis. B.01*, Gaussian, Inc., Wallingford CT, 2009.

5922 | *Inorg. Chem. Front.*, 2024, **11**, 5913–5923

This journal is © the Partner Organisations 2024

38 S. Dey, T. Sharma and G. Rajaraman, Unravelling the role of spin–vibrational coupling in designing high-performance pentagonal bipyramidal Dy(III) single ion magnets, *Chem. Sci.*, 2024, **15**, 6465–6477.

39 A. Schäfer, H. Horn and R. Ahlrichs, Fully optimized contracted Gaussian basis sets for atoms Li to Kr, *J. Chem. Phys.*, 1992, **97**, 2571–2577.

40 X. Cao and M. Dolg, Segmented contraction scheme for small-core actinide pseudopotential basis sets, *J. Mol. Struct.: THEOCHEM*, 2004, **673**, 203–209.

41 X. Cao and M. Dolg, Valence basis sets for relativistic energy-consistent small-core lanthanide pseudopotentials, *J. Chem. Phys.*, 2001, **115**, 7348–7355.

42 G. B. Bacskay, A Quardatically Convergent Hartree.Fock (QC-SCF) Method. Application to Closed Systems, *Chem. Phys.*, 1981, **61**, 385–404.

43 M. Reiher, Douglas–Kroll–Hess Theory: a relativistic electrons-only theory for chemistry, *Theor. Chem. Acc.*, 2006, **116**, 241–252.

44 B. O. Roos, R. Lindh, P. Å. Malmqvist, V. Veryazov and P. O. Widmark, Main Group Atoms and Dimers Studied with a New Relativistic ANO Basis Set, *J. Phys. Chem. A*, 2004, **108**, 2851–2858.

45 B. O. Roos, R. Lindh, P. Å. Malmqvist, V. Veryazov, P. O. Widmark and A. C. Borin, New Relativistic Atomic Natural Orbital Basis Sets for Lanthanide Atoms with Applications to the Ce Diatom and LuF₃, *J. Phys. Chem. A*, 2008, **112**, 11431–11435.

46 P. Å. Malmqvist, B. O. Roos and B. Schimmelpfennig, The restricted active space (RAS) state interaction approach with spin–orbit coupling, *Chem. Phys. Lett.*, 2002, **357**, 230–240.

This journal is © the Partner Organisations 2024

Inorg. Chem. Front., 2024, **11**, 5913–5923 | **5923**